Microstructural and crystallographic characteristics of interpenetrating and non-interpenetrating multiply twinned nanostructure in a Ni–Mn–Ga ferromagnetic shape memory alloy

D Y Cong, Y D Zhang, C Esling, Y D Wang, J.S. Lecomte, X Zhao, L Zuo

▶ **To cite this version:**

D Y Cong, Y D Zhang, C Esling, Y D Wang, J.S. Lecomte, et al.. Microstructural and crystallographic characteristics of interpenetrating and non-interpenetrating multiply twinned nanostructure in a Ni–Mn–Ga ferromagnetic shape memory alloy. Acta Materialia, 2011, 59 (18), pp.7070 - 7081. 10.1016/j.actamat.2011.07.062 . hal-03864499

HAL Id: hal-03864499

https://cnrs.hal.science/hal-03864499v1

Submitted on 26 Dec 2022

HAL is a multi-disciplinary open access archive for the deposit and dissemination of scientific research documents, whether they are published or not. The documents may come from teaching and research institutions in France or abroad, or from public or private research centers.

L'archive ouverte pluridisciplinaire **HAL**, est destinée au dépôt et à la diffusion de documents scientifiques de niveau recherche, publiés ou non, émanant des établissements d'enseignement et de recherche français ou étrangers, des laboratoires publics ou privés.

Microstructural and crystallographic characteristics of interpenetrating and non-interpenetrating multiply twinned nanostructure in a Ni–Mn–Ga ferromagnetic shape memory alloy

D.Y. Cong [a,b], Y.D. Zhang [a,b], C. Esling [b,*], Y.D. Wang [a], J.S. Lecomte [b], X. Zhao [a], L. Zuo [a,*]
[a]Key Laboratory for Anisotropy and Texture of Materials (Ministry of Education), Northeastern University, Shenyang 110004, China
[b]Laboratoire d'Étude des Microstructures et de Mécanique des Matériaux (LEM3), CNRS UMR 7239, Université Paul Verlaine – Metz, 57045 Metz, France
* Corresponding authors. Tel.: +33 3 87315390; fax: +33 3 87315377 (C. Esling). E-mail addresses: claude.esling@univ-metz.fr (C. Esling), lzuo@mail.neu.edu.cn (L. Zuo).

Abstract

A systematic investigation of microstructure and crystallography of the multiply twinned structure at the nanometer scale in a $Ni_{53}Mn_{25}Ga_{22}$ ferromagnetic shape memory alloy (FSMA) was performed. Nanoscale internal twins inside the micrometer-scale martensitic lamellae were observed. In each lamella, two nanotwin variants with a compound twinning relationship exist, and the twinning elements are $\mathbf{K_1} = \{112\}, \mathbf{K_2} = \{11\bar{2}\}, \boldsymbol{\eta_1} = \langle 11\bar{1}\rangle, \boldsymbol{\eta_2} = \langle 111\rangle, \mathbf{P} = \{1\bar{1}0\}$ and $s = 0.379$. Two types of lamellar interfaces, i.e., interpenetrated interlamellar interface and stepped intralamellar interface, were revealed. The orientation relationships between the nanotwins connected by these two types of interfaces were unambiguously determined, and it was found that the respective orientation relationship between the neighboring nanotwins depends strongly on the adjacency condition at the interfaces. The possible formation mechanisms of the interpenetrated interlamellar interface and stepped intralamellar interface are discussed. These results are useful for property optimization by microstructure control in the FSMAs.

Keywords

Ferromagnetic shape memory alloy, Nanotwins, Crystallography, Orientation relationship, Interface structure

1. Introduction

Shape memory alloys (SMAs) are attractive intelligent materials which have an intrinsic ability to recover their initial configuration upon phase transformation [1]. During the past few decades, great efforts have been made to investigate various aspects of SMAs [2], [3], [4], [5], owing to their wide applications in medical, aerospace and marine industries [1]. However, the working frequency of the conventional thermally controlled SMAs is relatively low because of the slow process of cooling and heating. This greatly limits their practical applications in certain fields. The newly developed ferromagnetic shape memory alloys (FSMAs) [6], [7], [8], [9], [10], [11], [12], [13], [14], [15] integrate the advantages of both conventional SMAs [1], [2], [3], [4], [5] and magnetostrictive materials [16], showing giant output strain and fast dynamic response [17], [18], which makes them extremely promising for use in sensors and actuators.

Increasing efforts have recently been devoted to revealing the new microstructural and crystallographic characteristics of FSMAs [12], [13], [19], [20], which are crucial to realizing their practical applications. It is well recognized that twins in martensite play an important

role in achieving excellent shape memory effect (SME) in both FSMAs and conventional SMAs (hereafter denoted as (F)SMAs) [17], [18]. Therefore, investigation of martensitic twins at different scales is of great significance. Although nanoscale twins in (F)SMAs have been observed in several studies [19], [20], [21], [22], [23], [24], [25], so far there has been no systematic and detailed investigation of the orientation relationships (especially misorientations) between the multiply twinned structures at the nanometer scale. What is more, the intrinsic nature of the nanotwins and the twin interfaces is still far from understood. The lack of fundamental crystallographic information has greatly hindered further attempts to develop high-performance (F)SMAs with large SME, excellent mechanical properties and high stability during cycling. A full understanding of the correlation between microstructure and crystallography of the nanotwins is therefore of great importance.

Ni–Mn–Ga alloys are the most intensively studied FSMAs, because they exhibit large magnetic-field-induced strain (MFIS) as a result of magnetic-field-induced twin boundary motion [9], [17], [18], [26], [27], [28], [29], [30], [31], [32], [33], [34], [35], [36]. Recently, it was found that the twin microstructure has a great influence on the twin boundary mobility of these alloys [37], [38]. To understand the underlying mechanism responsible for such influence, systematic microstructural and crystallographic characterization of the martensitic twins is therefore quite necessary. It is commonly recognized that there are three main types of martensite in Ni–Mn–Ga alloys: non-modulated (NM), five-layered modulated (5M) and seven-layered modulated (7M) martensites [39]. Owing to the complexity of the crystal structure of 5M and 7M martensites, detailed crystal structure information (e.g., space group and atomic occupations) is still under debate [40], [41], [42], [43], [44], and therefore it is very difficult to make precise and reliable crystallographic analyses of the twin structures in these martensites owing to the lack of precise crystal structure information. In contrast, accurate crystal structure information on NM martensite has been obtained by high-resolution neutron diffraction experiments [45], [46], which makes it possible to perform precise and reliable crystallographic analyses of the twin structures in NM martensite. On the other hand, it is well recognized that the crystal structures of NM, 5M and 7M martensites are closely related to each other. It is noteworthy that, with the concept of adaptive martensite [47], Kaufmann et al. [12] recently elucidated that the 7M martensite is a nanotwinned structure built from the NM martensitic unit cells, and the transition from 7M to NM martensite proceeds by a coarsening process [12]. Therefore, investigation of the microstructural and crystallographic characteristics of the nanotwins in NM martensite helps in understanding those characteristics in 5M and 7M martensites and therefore would facilitate the improvement of MFIS observed in 5M and 7M martensites. That is why a Ni–Mn–Ga alloy with NM martensite was investigated in the present work.

Actually, while the twin boundaries in 5M and 7M martensites are known to be highly mobile, the twin boundary mobility in NM martensite has been considered, for a long time, to be low. However, Chernenko et al. [48] recently observed a MFIS of ~0.2% in NM martensite, clearly evidencing significant magnetic-field-induced twin boundary motion in NM martensite. Moreover, stress-assisted MFIS has also been successfully achieved in NM martensite [49], [50], [51], making it promising for practical applications. In fact, the NM martensite which is formed as a ground state of the Heusler-type FSMAs [48] has many advantages over 5M and 7M martensites, including high stability, good chemical properties and high ductility [48]. Consequently, in addition to the potential use as FSMAs, the alloys with NM martensite can also be used as conventional high-temperature SMAs [52], [53], [54], [55], [56].

The present paper reports on the systematic study of the microstructural and crystallographic characteristics of the multiply twinned nanostructure in a $Ni_{53}Mn_{25}Ga_{22}$ (at.%) alloy with NM martensitic structure. Nanoscale internal twins were found inside the micrometer-scale martensitic lamellae, the intrinsic nature of the interpenetrated interlamellar and stepped intralamellar interfaces were elucidated, and the orientation relationships between the nanotwins were revealed for the first time. Such new findings will be instructive for developing high-performance (F)SMAs by microstructure control.

2. Experimental

A 70-g button ingot of $Ni_{53}Mn_{25}Ga_{22}$ (at.%) was prepared by repeated melting of the high-purity constituent elements in an arc furnace. The phase transformation temperatures and crystal structure of the alloy were determined by differential scanning calorimetry (DSC) and neutron powder diffraction, respectively. DSC measurement shows that the martensitic and reverse transformation start and finish temperatures, M_s, M_f, A_s and A_f are 386 K, 368 K, 408 K and 424 K, respectively. High-resolution neutron powder diffraction reveals that this alloy has a tetragonal NM martensitic structure at room temperature, with a = 3.865 Å, c = 6.596 Å and c/a = 1.707. The space group is $I4/mmm$ (No. 139), with Ni, Mn and Ga atoms occupying 4d (0, 0.5, 0.25), 2b (0, 0, 0.5) and 2a (0, 0, 0) Wyckoff sites, respectively (Fig. 1c). The detailed description of this structure is given in Refs. [45], [46]. It should be noted that two different unit cells are used in the literature to describe the crystal structure of NM martensite. One is directly constructed from the cubic axes of austenite (Fig. 1a and b) (hereafter denoted as UCM′), and the other is constructed from the principal axes of martensite (Fig. 1c) (denoted as UCM). For the alloy in this study, UCM′ is produced roughly by a 6.40% contraction along two cubic axes (which become a' in UCM′) and a 12.95% extension along a third perpendicular cubic axis (which becomes c' in UCM′) of the unit cell of austenite (UCA) (Fig. 1a and b). The orientation relationship between UCM′ and UCM can be described as $(0\ 0\ 1)_{UCM'}//(0\ 0\ 1)_{UCM}$ and $[1\ 0\ 0]_{UCM'}//[1\ 1\ 0]_{UCM}$, with $a' = \sqrt{2}a$ and $c' = c$ (Fig. 1d). From the crystallographic point of view, it is more reasonable to choose UCM, because it involves a smaller unit cell volume. However, for a simple description of the strain values induced by stress, magnetic field or temperature change, UCM′ is commonly used in the literature, because its basic lattice vectors are closely related to the easy and hard magnetization axes of martensite, and it directly reflects the lattice parameter changes with respect to UCA. In order to make precise crystallographic analyses, UCM (Fig. 1c) is selected for the present study.

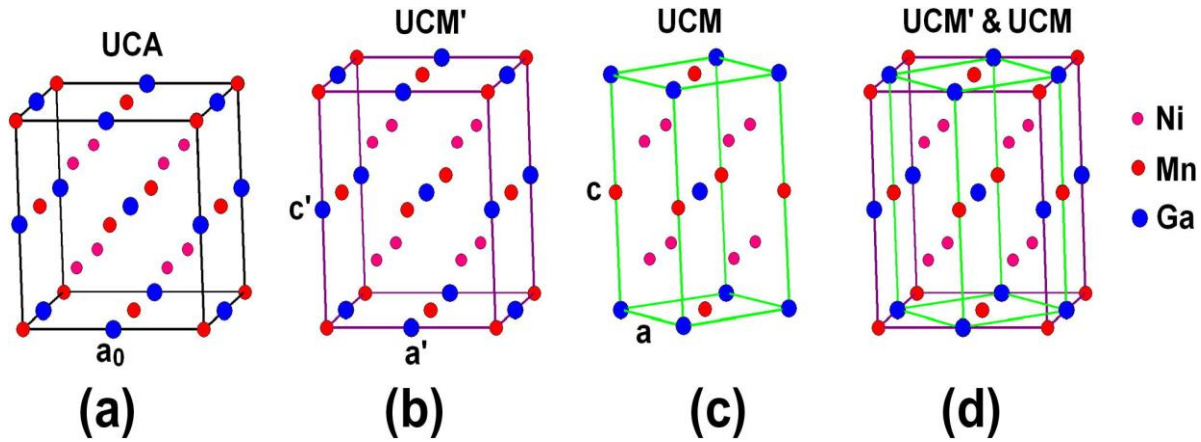

Fig. 1. (a) Unit cell of austenite (cubic, a_0 = 5.840 Å), (b) unit cell of martensite commonly used in literature (tetragonal, a' = 5.466 Å, c' = 6.596 Å, c'/a' = 1.207), (c) unit cell of

martensite used in the present study (tetragonal, a = 3.865 Å, c = 6.596 Å, c/a = 1.707), and (d) illustration of the relationship between the unit cells in (b and c).

A 12 × 6 × 3 mm^3 sample was cut from the ingot. It was further annealed at 1173 K for 4 h, followed by slow furnace cooling in order to reduce the internal stress generated during cooling, especially during the transformation from austenite to martensite. The transformed microstructure was observed by high-resolution scanning electron microscopy (SEM) with a JEOL JSM 6500F instrument equipped with a field emission gun (FEG-SEM) in the backscattered electron (BSE) imaging mode, and the detailed microstructures at the interlamellar and intralamellar interfaces were examined by transmission electron microscopy (TEM) with a Philips CM 200 instrument. The orientations (expressed in terms of Euler angles) of the microstructural constituents were determined by manually acquiring and indexing the electron backscattered diffraction (EBSD) [26], [27], [38], [57], [58], [59], [60], [61], [62], [63] Kikuchi patterns using the FEG-SEM equipped with Oxford-HKL's Channel 5 software. The orientation relationships between the microstructural constituents were determined by misorientation calculation [64], and the interface plane was determined by the indirect two-trace method [65].

3. Results and discussion

3.1. Microstructural characteristics

The microstructure of the $Ni_{53}Mn_{25}Ga_{22}$ alloy is shown in Fig. 2. It can be seen from the SEM-BSE image in Fig. 2a that this alloy has a typical lamellar martensitic microstructure at room temperature. The martensitic lamellae, with a thickness of several micrometers, are well self-accommodated and separated from each other by straight interlamellar boundaries. However, the lamellae often bifurcate or bend through reorientation. The intralamellar reorientation can be readily seen from the contrast change of the image, as the contrast of the SEM-BSE image originates from the crystal orientation in the case of single phase with a homogeneous composition in the studied alloy.

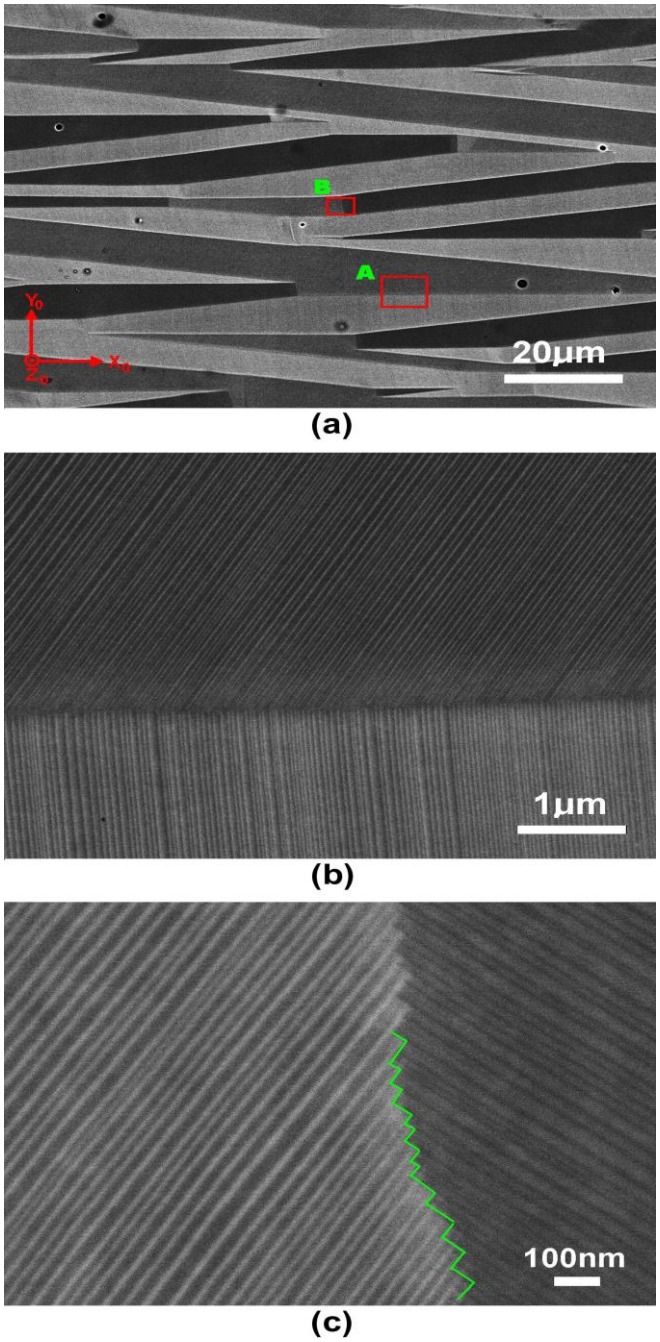

Fig. 2. Microstructure of $Ni_{53}Mn_{25}Ga_{22}$ alloy: (a) BSE image showing a self-accommodated lamellar microstructure, and the sample coordinate system $X_0Y_0Z_0$ for EBSD measurement. Frames A and B display the interlamellar interface and intralamellar interface, respectively. (b) Zoom image of frame A in (a), showing the nanoplates in two neighboring lamellae. (c) Zoom image of frame B in (a), demonstrating the "step" configuration of the intralamellar interface; solid lines are drawn to underline the stepped interface. All the micrographs were taken from the cross section spanned by the X_0 and Y_0 directions, with X_0 parallel to the width (6 mm) and Y_0 parallel to the thickness (3 mm) of the sample.

High-magnification observation demonstrates that the martensitic lamellae are composed of a vast number of fine internal plates with two contrasts distributed alternately, as shown in Fig. 2b (the zoom image of frame A in Fig. 2a). The two distinct contrasts indicate that the internal plates in each lamella have only two orientations, suggesting that they might be twin-related (this will be verified later). The thickness of the internal plates ranges from several

nanometers to several tens of nanometers. The nanoplates are paired, and clearly the two nanoplates in each pair have quite different thicknesses. One is thicker (major) and the other is thinner (minor). The interfaces between the nanoplates are straight, sweeping the whole lamella. High-magnification SEM observation also reveals that the intralamellar interface that borders the straight lamella with its bent part is not straight and has a "step" configuration consisting of well-defined fine steps, as shown in Fig. 2c (the zoom image of frame B in Fig. 2a). In the "step" configuration, one bundle of nanoplates from a lamella ends at the intralamellar interface and this forms one step. The microstructure with internal twins inside martensitic lamellae was also observed in a $Ni_{52.8}Mn_{25.7}Ga_{21.5}$ single crystal with NM structure [66], but the internal twins are at the micrometer scale, much thicker than those observed in the present study.

3.2. Twinning relationship and twin interface between internal nanotwins

As the internal nanoplates in the martensitic lamellae are very fine, it is quite difficult to determine their orientations by automatic EBSD measurement, which proves to be efficient in characterizing the micrometer-scale martensitic lamellae in Ni–Mn–Ga alloys [26], [27], [38], [60], [61], [62], [63]. Fortunately, by optimizing the probe current and the plate orientation with respect to the incident electron beam, clear EBSD Kikuchi patterns of these nanoplates (even the minor ones) were manually acquired and indexed to obtain their orientation information. Fig. 3a shows the EBSD Kikuchi pattern acquired from one of the nanoplates, and Fig. 3b shows the pattern recalculated using the tetragonal crystal structure information shown in Fig. 1c for the indexation of the pattern in Fig. 3a. Clearly, the EBSD Kikuchi pattern is well indexed, confirming that, on the one hand, the crystal structure information determined from neutron diffraction is accurate and, on the other hand, the manual EBSD measurement is efficient in identifying the orientations of the nanoplates.

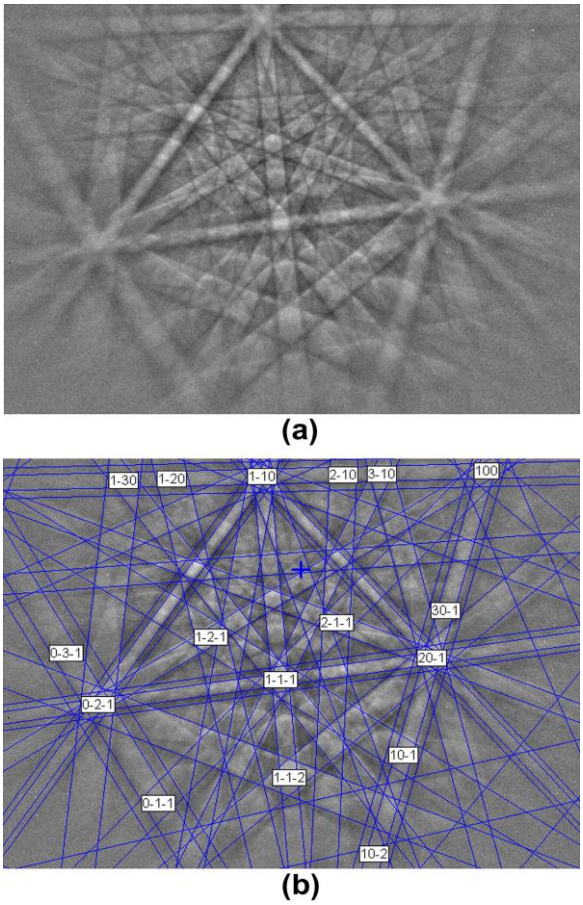

Fig. 3. (a) Kikuchi pattern acquired from one of the nanoplates and (b) its indexation using the crystal structure information shown in Fig. 1c.

In order to determine the orientation relationship between the adjacent nanoplates, their misorientations were calculated. The misorientation between two crystals is usually expressed by rotation mapping the first crystal into the second one. This rotation is parameterized by the misorientation (or rotation) angle and the corresponding rotation axis. As mentioned above, the martensite of the $Ni_{53}Mn_{25}Ga_{22}$ alloy has a tetragonal structure [45]. Owing to the tetragonal symmetry (with eight symmetry elements), 64 possible symmetry equivalent misorientations between two specific crystals with tetragonal structure can be obtained. These 64 possible symmetry equivalent misorientations can be finally reduced into eight sets of misorientation angles and axes (see Ref. [64] for details). In each set, there is one misorientation angle with a family of eight corresponding rotation axes equivalent through the rotation point symmetry group [64]. According to the definition of twinning [67], [68], [69], [70], if there are two 180° rotations around two rational axes and the planes normal to the rotation axes are also rational, the two crystals have a compound twinning relationship, with one rotation axis being the twinning direction $\boldsymbol{\eta}_1$, and the other being the normal of the twinning plane $\mathbf{K}_1$. By taking into account the criterion of minimum twinning shear, all the twinning elements ($\mathbf{K}_1$, $\boldsymbol{\eta}_1$, the conjugate twinning plane $\mathbf{K}_2$, the conjugate twinning direction $\boldsymbol{\eta}_2$, the plane of shear $\mathbf{P}$, and the magnitude of shear s) can be determined [71]. The detailed steps for determining the twinning elements can be found in a recent paper [64]. With misorientation calculation [64] (some results are displayed in Table 1), the internal nanoplates within each lamella are found to have a compound twinning relationship with the twinning elements $\mathbf{K_1} = \{112\}, \mathbf{K_2} = \{11\bar{2}\}, \boldsymbol{\eta_1} = \langle 11\bar{1}\rangle, \boldsymbol{\eta_2} = \langle 111\rangle, \mathbf{P} = \{1\bar{1}0\}$ and $s = 0.379$. These internal nanotwins are related to each other by a rotation of ~79° around the $\langle 1\ 1\ 0\rangle$ axis (Table 1). This is different from the misorientation (~86° around the $\langle 1\ 1\ 0\rangle$ axis)

between the micrometer-scale twins in Ni–Mn–Ga alloys with 5M structure [26], [27], [62], [72].

Table 1. Minimum misorientation angle and the two near-180° misorientation angles, with their corresponding rotation axes, between the internal nanotwins and the nanotwins connected by the interlamellar interface as illustrated in Fig. 4a; for each misorientation angle ω, there is a family of eight equivalent rotations with eight corresponding equivalent axes **d**, which transform into each other according to the tetragonal rotation symmetry group.

Pair of nanotwins	Misorientation angle, ω (°)	Rotation axis, **d**			
		d_1	d_2	d_3	
V1/V2	79.4	0.7030	0.7111	0.0114	0.7° from ⟨1 1 0⟩ direction
	179.2	0.4541	0.4490	0.7695	0.2° from ⟨1 1 1⟩ direction
	179.6	0.5390	0.5493	0.6386	0.4° from the normal of {1 1 2} plane
V3/V4	79.2	0.7062	0.7080	0.0003	0.1° from ⟨1 1 0⟩ direction
	179.9	0.5448	0.5445	0.6377	0.0° from the normal of {1 1 2} plane
	180.0	0.4515	0.4504	0.7703	0.1° from ⟨1 1 1⟩ direction
V1/V3	83.0	0.6688	0.7434	0.0049	3.0° from ⟨1 1 0⟩ direction
	176.0	0.5276	0.5322	0.6621	1.8° from the normal of {1 1 2} plane
	179.6	0.4926	0.4432	0.7490	2.7° from ⟨1 1 1⟩ direction
V2/V4	13.4	0.9053	0.0577	0.4209	3.8° from ⟨4 0 1⟩ direction
	174.4	0.0067	0.1054	0.9944	6.1° from ⟨0 0 1⟩ direction
	179.2	0.0490	0.9932	0.1053	6.7° from the normal of {0 1 0} plane
V1/V4	88.0	0.6034	0.7974	0.0078	7.9° from ⟨1 1 0⟩ direction
	169.1	0.5147	0.5070	0.6914	4.1° from the normal of {1 1 2} plane
	179.4	0.5541	0.4193	0.7191	6.8° from ⟨1 1 1⟩ direction
V2/V3	88.8	0.7884	0.6151	0.0098	7.1° from ⟨1 1 0⟩ direction
	170.2	0.5120	0.5022	0.6969	4.6° from the normal of {1 1 2} plane
	179.2	0.4304	0.5516	0.7145	6.7° from ⟨1 1 1⟩ direction

Note: The rotation axes are expressed in coordinates; the *c*/*a* ratio should be taken into account when transforming the coordinates into the Miller indices.

With the direction vectors of the trace of the twin interface and the individual orientations of the twins, it is possible to determine the twin interface plane by the indirect two-trace method described in Ref. [65]. The calculated results show that the twin interface plane between the internal nanotwins is {0.4084 0.4086 0.8163} when expressed in the tetragonal crystal coordinate system [45], which is actually the {1 1 2} plane. The fact that the interface plane coincides with the twinning plane indicates that the twin interfaces between the nanotwins are coherent on the {1 1 2} twinning plane, which ensures the minimization of the interfacial energy. Obviously, the alternate formation of the internal nanotwins is the requirement of the invariant lamellar interface, that is, during martensitic transformation the total accumulated strain at the lamellar interface is zero, which can be achieved by adjusting the thickness of the nanotwins [73].

3.3. Inter-lamellar interface and orientation relationships between the nanotwins connected by such interface

The adjacencies of the nanotwins at the straight interlamellar interfaces (Fig. 2b) and the stepped intralamellar interfaces (Fig. 2c) represent two types of crystallographic connections. These connections result in different orientation relationships between those neighboring pairs of nanotwins across the interfaces. So far, such orientation relationships have not been reported, and the discovery of them undoubtedly provides new insights into the crystallography of FSMAs. For clear presentation, the two types of configurations are analyzed separately in the present and following subsections.

For the interlamellar connection, Fig. 4a illustrates the nanotwins (V1 and V2 in lamella A and V3 and V4 in lamella B) connected by the interlamellar interface, and Fig. 4b displays the {1 1 2} and ⟨1 1 1⟩ standard stereographic projections (in the crystal coordinate system of V1) of the four nanotwin variants, together with a sketch of the unit cell with (1 1 2) plane and

direction. As shown in Fig. 4b, the intersecting angles between the twinning planes and between the twinning directions of the nanotwins in lamella A and lamella B are 119.6° and 112.7°, respectively. This geometrical configuration offers four possible adjacencies (V1 and V3, V1 and V4, V2 and V3, V2 and V4) between the respective nanotwins in lamella A and lamella B. Table 1 displays the misorientation calculation results of the minimum misorientation angle and two near-180° misorientation angles between those adjacent nanotwins, with their corresponding rotation axes. As a reference, the same misorientation information from the internal nanotwin pairs (V1 and V2, V3 and V4) is also given in the table. It is revealed that, when the major nanotwin variants V1 and V3 meet, these two variants are still twin-related, with the twinning elements of the same family as those of the internal nanotwins, i.e., . Indirect two-trace method calculation shows that the interlamellar interface plane is in general agreement with the {1 1 2} twinning plane. However, the corresponding {1 1 2} planes of the variants V1 and V3 have a deviation of 3.6° and the corresponding ⟨1 1 1⟩ directions have a deviation of 5.5°, as demonstrated in Table 2a. This suggests that the twinning relationship between V1 and V3 is not perfect. The imperfectness of the twinning relationship results in the fact that these two variants are related to each other by a rotation of 83.0° around the ⟨1 1 0⟩ axis, rather than a rotation of ~79° between the internal nanotwins (e.g., V1 and V2) (Table 1). When the major and minor variants (V1 and V4, V2 and V3) meet, the {1 1 2} twinning relationship suffers an enlarged imperfectness (Table 2a). The corresponding {1 1 2} planes and corresponding ⟨1 1 1⟩ directions (of V1 and V4) deviate by 8.2° and 13.7°, respectively (Table 2a). The major and minor variants are related to each other by a rotation of ~88° around roughly the ⟨1 1 0⟩ axis. Notably, when the minor variants V2 and V4 meet, the twinning relationship is totally lost. They are only related to each other by a rotation of 13.4° around the ⟨ 0.9630 0.0614 0.2623⟩ (3.8° from ⟨4 0 1⟩) axis. The above results show that the twinning relationship between the internal twins is perfect, while that between the lamellae is imperfect. This indicates that the perfect twinning relationships between the internal nanotwins and between the lamellae cannot be satisfied at the same time, and the internal twins have the higher priority.

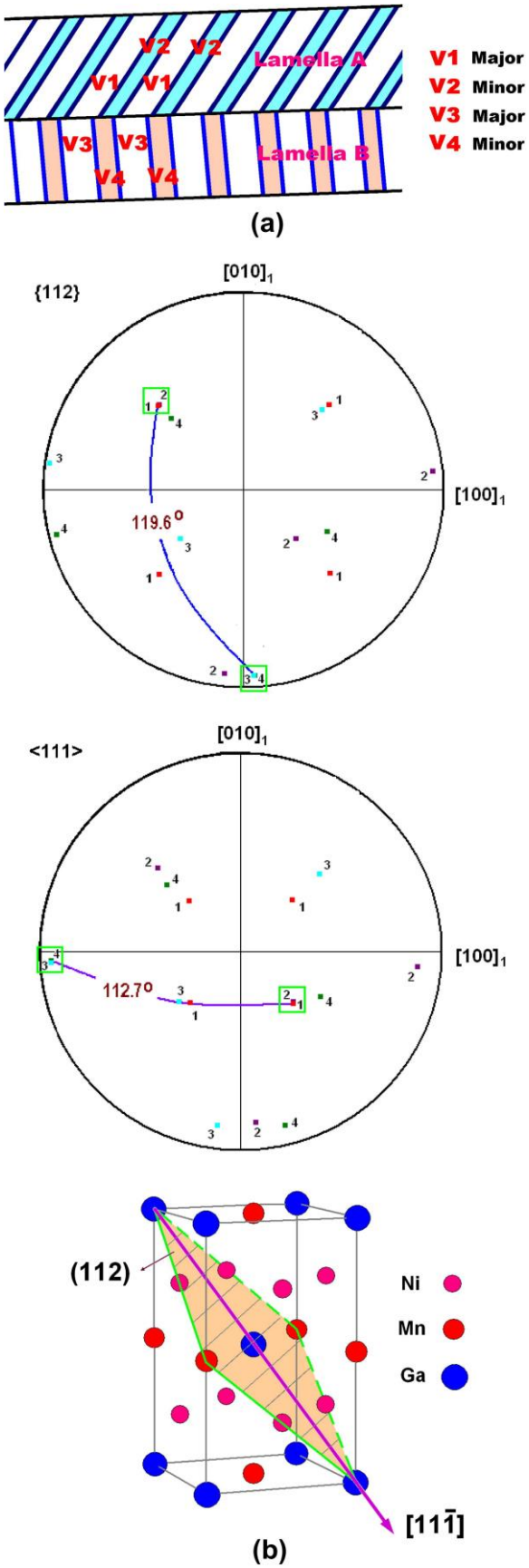

Fig. 4. (a) Schematic illustration of the nanotwins connected by the interlamellar interface shown in Fig. 2b. (b) {1 1 2} and 〈1 1 1〉 standard stereographic projections, in the crystal coordinate system of V1, of the individual orientations of the nanotwins in (a). The

number *i* (*i* = 1, 2, 3, 4) in the projections corresponds to the orientation of each variant V*i*. According to the tetragonal symmetry of the martensitic structure, each nanotwin variant has four crystallographically equivalent {1 1 2} planes and ⟨1 1 1⟩ directions, respectively. Thus, there are four poles corresponding to each nanotwin orientation (so that each number *i* appears four times) in the respective {1 1 2} and ⟨1 1 1⟩ standard stereographic projections. The common {1 1 2} planes (twinning planes) and ⟨1 1 1⟩ directions (twinning directions) of the internal nanotwins are enclosed in the squares. A sketch of the unit cell with (1 1 2) plane and direction is included in (b) to help visualize orientations

Table 2. (a) Orientation relationships, expressed in terms of parallel planes and directions, between the nanotwins connected by the interlamellar interface as illustrated in Fig. 4a; (b and c) planes and directions in nanotwin variants V1 (b) and V2 (c) before and after the shear introduced by the penetration of V4 at the interpenetrated interlamellar interface as illustrated in Fig. 5b; subscript *i* (*i* = 1, 2, 3, 4) in the indices denotes that these indices are expressed with respect to the crystal coordinate system of V*i*.

Pair of nanotwins	Orientation relationship	
(a)		
V1/V2	$(\bar{1}\,1\,2)_1//(1\,\bar{1}\,2)_2$	$[1\,\bar{1}\,1]_1//[1\,\bar{1}\,1]_2$
V3/V4	$(1\,\bar{1}\,2)_3//(\bar{1}\,1\,2)_4$	$[\bar{1}\,1\,1]_3//[\bar{1}\,\bar{1}\,\bar{1}]_4$
V1/V3	$(1\,1\,2)_1$ 3.6° from $(\bar{1}\,\bar{1}\,2)_3$	$[\bar{1}\,\bar{1}\,1]_1$ 5.5° from $[1\,1\,1]_3$
V1/V4	$(1\,\bar{1}\,\bar{2})_1$ 8.2° from $(1\,\bar{1}\,2)_4$	$[1\,\bar{1}\,1]_1$ 13.7° from $[\bar{1}\,1\,1]_4$
V2/V3	$(1\,1\,2)_2$ 9.1° from $(\bar{1}\,1\,\bar{2})_3$	$[1\,1\,\bar{1}]_2$ 13.4° from $[1\,\bar{1}\,\bar{1}]_3$
V2/V4	Related to each other by a rotation of 13.4° around the ⟨0.9630 0.0614 0.2623⟩ axis	

Plane before shear	Plane after shear	Direction before shear	Direction after shear
(b)			
$(1\,1\,2)_1$	$(0.9810\ 1.3661\ 1.9235)_1$ (9.5° from $(1\,1\,2)_1$)	$[\bar{1}\,\bar{1}\,1]_1$	$[\overline{0.5665}\ \overline{0.9805}\ 0.9853]_1$ (10.6° from $[\bar{1}\,\bar{1}\,1]_1$)
$(\bar{1}\,1\,2)_1$	$(\overline{0.9801}\ 0.6167\ 2.0801)_1$ (11.6° from $(\bar{1}\,1\,2)_1$)	$[1\,\bar{1}\,1]_1$	$[1.4725\ \overline{0.9788}\ 0.9840]_1$ (10.3° from $[1\,\bar{1}\,1]_1$)
$(\bar{1}\,\bar{1}\,2)_1$	$(\overline{0.9783}\ \overline{1.4169}\ 2.0872)_1$ (9.3° from $(\bar{1}\,\bar{1}\,2)_1$)	$[1\,1\,1]_1$	$[0.7231\ 0.9876\ 1.0094]_1$ (6.8° from $[1\,1\,1]_1$)
$(1\,\bar{1}\,2)_1$	$(0.9827\ \overline{0.6676}\ 1.9305)_1$ (9.0° from $(1\,\bar{1}\,2)_1$)	$[\bar{1}\,1\,1]_1$	$[\overline{1.3159}\ 0.9858\ 1.0107]_1$ (6.7° from $[\bar{1}\,1\,1]_1$)
(c)			
$(1\,1\,2)_2$	$(1.0534\ 1.0492\ 2.1403)_2$ (0.5° from $(1\,1\,2)_2$)	$[\bar{1}\,\bar{1}\,1]_2$	$[\overline{1.0528}\ \overline{1.0840}\ 1.0496]_2$ (0.7° from $[\bar{1}\,\bar{1}\,1]_2$)
$(\bar{1}\,1\,2)_2$	$(\overline{1.0961}\ 0.9115\ 1.7475)_2$ (5.7° from $(\bar{1}\,1\,2)_2$)	$[1\,\bar{1}\,1]_2$	$[0.7977\ \overline{1.3218}\ 1.1898]_2$ (9.0° from $[1\,\bar{1}\,1]_2$)
$(\bar{1}\,\bar{1}\,2)_2$	$(\overline{1.3339}\ \overline{1.3076}\ 1.1227)_2$ (20.3° from $(\bar{1}\,\bar{1}\,2)_2$)	$[1\,1\,1]_2$	$[0.6600\ 0.4592\ 1.3190]_2$ (20.6° from $[1\,1\,1]_2$)
$(1\,\bar{1}\,2)_2$	$(0.8156\ \overline{1.1698}\ 1.5155)_2$ (11.3° from $(1\,\bar{1}\,2)_2$)	$[\bar{1}\,1\,1]_2$	$[\overline{1.1905}\ 0.6970\ 1.1787]_2$ (10.2° from $[\bar{1}\,1\,1]_2$)

The detailed fine microstructure at the interlamellar interface is shown in Fig. 5a. It is interesting to see that the interlamellar interface that is straight at the micrometer scale (Fig. 2a) shows a kind of grid structure in the TEM image (Fig. 5a), which means that the nanotwins in the two neighboring lamellae penetrate, to some extent, into each other. As the volume of the interpenetrated parts is relatively small, it is difficult to determine the orientation relationships between the neighboring penetrated and non-penetrated parts using selected area electron diffraction, owing to the insufficient diffraction. Calculation would be a potential alternative to determine the orientation relationships and to explain the formation mechanism of the interpenetrated interlamellar interface.

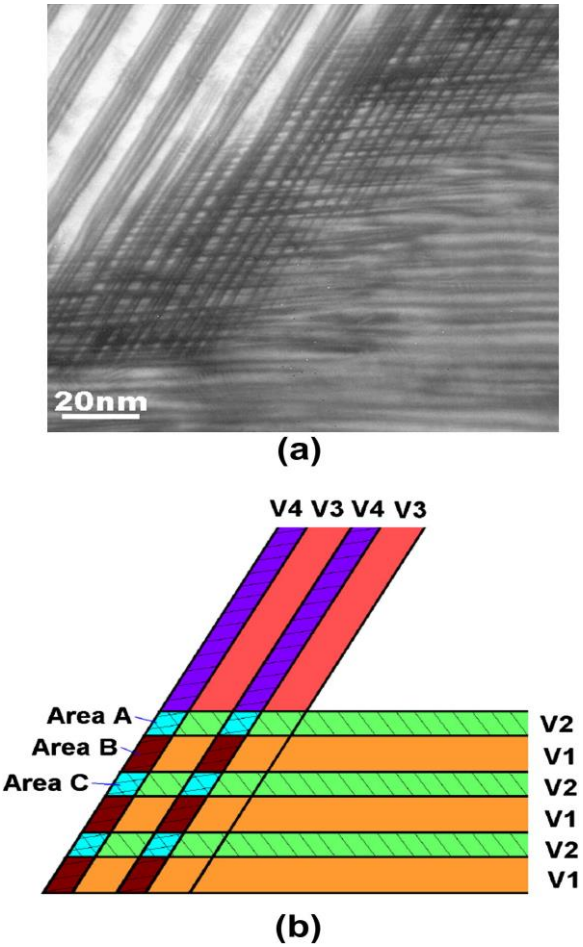

Fig. 5. (a) TEM image showing the detailed microstructure at the interpenetrated interlamellar interface. (b) Schematic illustration of the formation mechanism of the interpenetrated interlamellar interface shown in (a).

As the twinning deformation is relative between the twinned part and the undeformed matrix, it is assumed that the minor variants V2 and V4 are the twinned parts with respect to the undeformed matrix, the major variants V1 and V3, respectively. Thus, the crystal deformation of V4 can be described by a matrix **F** expressed in the crystal coordinate of V3. It is further assumed that V4 penetrates into V1 and V2, i.e., V1 and V2 suffer the twinning deformation of V4. This deformation displaces a vector **u** which lies in a plane whose normal is initially **h** in V*i* (*i* = 1, 2) to a new vector **v** within a plane whose normal is **k** in the same coordinate system [74]:

$$\begin{aligned} \mathbf{v} &= \mathbf{F_i u} \\ \mathbf{k} &= (\mathbf{F_i^{-1}})^{\mathrm{T}} \mathbf{h} \end{aligned} \qquad \mathbf{i} = 1, 2 \qquad (1)$$

where the superscripts −1 and T denote the inverse and transpose of a matrix, respectively. $\mathbf{F_i} = \mathbf{Q_i F Q_i^T}$, where $\mathbf{Q_i}$ is the coordinate transformation matrix transforming the tetragonal crystal coordinate system of V3 into that of V*i* (*i* = 1, 2). If the penetrated part of V*i* (*i* = 1, 2) assumes a twinning relationship with the non-penetrated part, the twinning plane and the twinning direction should be kept invariant. Calculations show that there indeed exist one {1 1 2} plane and one in-plane $\langle 11\bar{1} \rangle$ direction remaining more or less invariant. The {1 1 2} planes and $\langle 11\bar{1} \rangle$ directions in V1 and V2 before and after the deformation introduced by the penetration of V4 are listed in Table 2b and c, respectively. It is seen from Table 2c that,

when V4 penetrates into V2 (illustrated as area A in Fig. 5b) at the interlamellar interface, the penetrated part in V2 possesses an invariant plane and an in-plane direction ($(112)_2$ and $[\bar{1}\bar{1}2]_2$), indicating that the penetrated and the non-penetrated parts in V2 are also t2win-related. This offers the possibility for penetration. Using the new shear elements (plane and in-plane direction) to penetrate further into V1 (area B in Fig. 5b), although no invariant exact {1 1 2} plane and in-plane $\langle 11\bar{1}\rangle$ direction are kept, there is one pair quite close to $(11\bar{2})_1$(with 5.8° deviation) and $[1\ 1\ 1]_1$ (with 7.9° deviation) (for clarity, not shown). This suggests that the penetrated part and the non-penetrated part in V1 possess a deteriorated {1 1 2} twinning relationship. If V4 continues to penetrate into V2 (area C in Fig. 5b) with the new shear plane $(11\bar{2})_1$ and shear direction $[1\ 1\ 1]_1$, it is interesting to see the repetition of the $(1\ 1\ 2)_2$ plane (with 6.9° deviation) and $[\bar{1}\bar{1}1]_2$ direction (with 6.9° deviation) (not shown) as a kind of invariant plane and direction. This repetition offers the possibility of a continuous penetration, and the deterioration of the twinning relationship imposes a kind of hindrance to the penetration. As a consequence, the penetration weakens and finally stops after a certain number of repetitions, as seen in Fig. 5a. The occurrence of this interpenetration may be due to the high symmetry of the tetragonal structure. The high multiplicity of the {1 1 2} plane and the $\langle 11\bar{1}\rangle$ direction offers a high chance of multiple twinning.

3.4. Intra-lamellar interface and orientation relationships between the nanotwins connected by such interface

For the intralamellar connection, Fig. 6a illustrates the nanotwins (V1′ and V2′ in zone I and V3′ and V4′ in zone II) connected by the intralamellar interface, and Fig. 6b displays the {1 1 2} and $\langle 1\ 1\ 1\rangle$ standard stereographic projections (in the crystal coordinate system of V1′) of the four twin variants, together with a sketch of the unit cell with (1 1 2) plane and $[11\ \bar{1}]$ direction. It can be seen that the intersecting angle between the twinning planes of the nanotwins in zone I and zone II is 94.8°, and that between the twinning directions is 85.0°, different from the case at the interlamellar interface. Nevertheless, the intralamellar interface configuration also offers four possible adjacencies (V1′ and V3′, V2′ and V4′, V1′ and V4′, V2′ and V3′) between the nanotwins in the two zones. When the major variants (V1′ and V3′) meet, although there are two 180° rotations between them (see the misorientation calculation results displayed in Table 3), the plane {0 0 1} and direction $\langle 1\ 1\ 0\rangle$ corresponding to the rotation axes of the two 180° rotations are intrinsic symmetry elements of the tetragonal structure. According to the classical definition of twinning [67], [68], [69], [70], [75], these two variants are not twin-related, but only related to each other by a rotation of 5.9° roughly around the $\langle 1\ 1\ 0\rangle$ axis (Table 3). This slight crystallographic reorientation of nanotwins changes the direction of the interlamellar interface. Similarly, when the two minor variants (V2′ and V4′) meet, the orientation relationship between them is expressed by the same kind of rotation, but with a larger angle (15.8°around the $\langle 1\ 1\ 0\rangle$ axis). These two small rotations between the major variants (V1′ and V3′) and the minor variants (V2′ and V4′) render the major variant in one zone and the minor variant in the other zone (V1′ and V4′, V2′ and V3′) to be twin-related with the twinning elements of the same family as those of the internal nanotwins, as shown in Table 4a. Nevertheless, this twinning relationship also suffers some crystallographic imperfectness (the corresponding {1 1 2} planes and $\langle 1\ 1\ 1\rangle$ directions in V1′ and V4′ both deviate by 5.7°). Obviously, the combination of these orientation relationships between the nanotwin variants leads to the reorientation of the martensitic lamellae to achieve the self-accommodation of the lamellar microstructure.

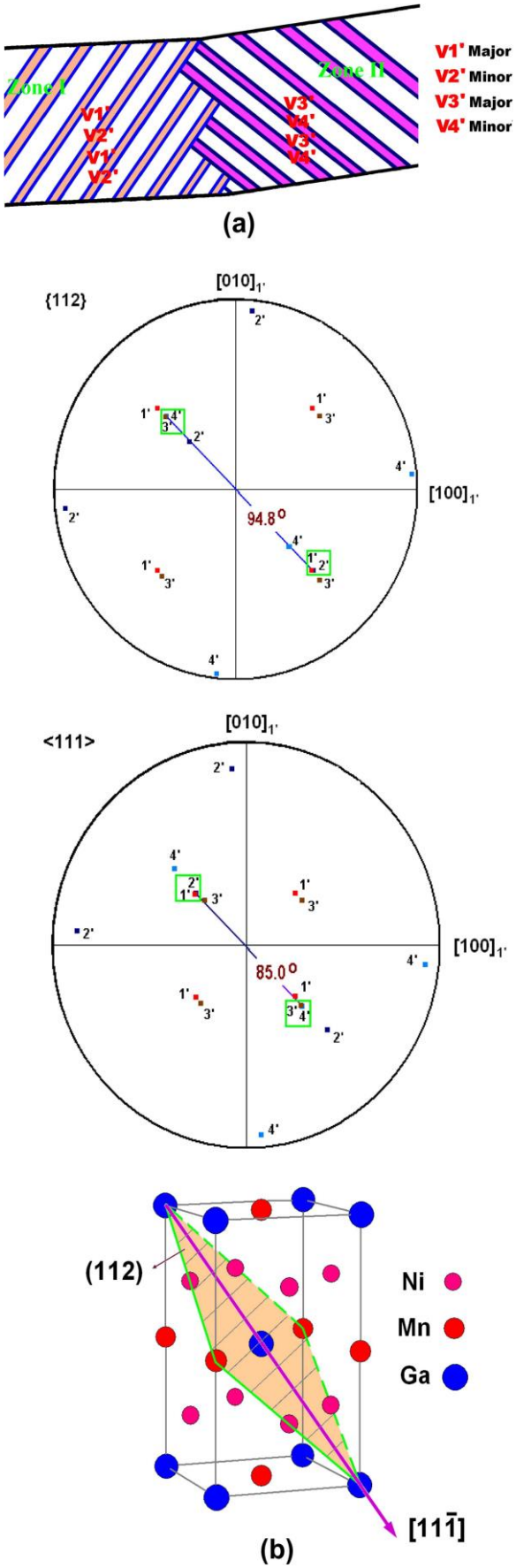

Fig. 6. (a) Schematic illustration of the nanotwins connected by the intralamellar interface shown in Fig. 2c. (b) {1 1 2} and 〈1 1 1〉 standard stereographic projections, in the

crystal coordinate system of V1′, of the individual orientations of the nanotwins in (a). The number i' (i' = 1′, 2′, 3′, 4′) in the projections corresponds to the orientation of each variant Vi'. According to the tetragonal symmetry of the martensitic structure, each nanotwin variant has four crystallographically equivalent {1 1 2} planes and ⟨1 1 1⟩ directions, respectively. Thus, there are four poles corresponding to each nanotwin orientation (so that each number i' appears four times) in the respective {1 1 2} and ⟨1 1 1⟩ standard stereographic projections. The common {1 1 2} planes (twinning planes) and ⟨1 1 1⟩ directions (twinning directions) of the internal nanotwins are enclosed in the squares. A sketch of the unit cell with (1 1 2) plane and direction is included in (b) to help visualize orientations.

Table 3. Minimum misorientation angle and the two near-180° misorientation angles, with their corresponding rotation axes, between the internal nanotwins and the nanotwins connected by the intralamellar interface as illustrated in Fig. 6a; for each misorientation angle ω, there is a family of eight equivalent rotations with eight corresponding equivalent axes **d** which transform into each other according to the tetragonal rotation symmetry group.

Pair of nanotwins	Misorientation angle, ω (°)	Rotation axis, **d**			
		d_1	d_2	d_3	
V1′ and V2′	79.2	0.7061	0.7082	0.0006	0.1° from ⟨1 1 0⟩ direction
	179.9	0.5449	0.5444	0.6377	0.0° from the normal of {1 1 2} plane
	180.0	0.4516	0.4503	0.7703	0.1° from ⟨1 1 1⟩ direction
V3′ and V4′	79.2	0.7053	0.7089	0.0018	0.2° from ⟨1 1 0⟩ direction
	179.8	0.5456	0.5440	0.6375	0.1° from the normal of {1 1 2} plane
	179.9	0.4519	0.4496	0.7705	0.1° from ⟨1 1 1⟩ direction
V1′ and V3′	5.9	0.7257	0.6672	0.1680	10.0° from ⟨1 1 0⟩ direction
	179.0	0.0342	0.0372	0.9987	2.9° from the normal of {0 0 1} plane
	179.8	0.7001	0.7123	0.0505	2.9° from ⟨1 1 0⟩ direction
V2′ and V4′	15.8	0.7453	0.6667	0.0093	3.2° from ⟨1 1 0⟩ direction
	179.1	0.6995	0.7013	0.1371	7.9° from the normal of {1 1 0} plane
	179.9	0.0915	0.1023	0.9905	7.9° from ⟨0 0 1⟩ direction
V1′ and V4′	85.0	0.7129	0.7012	0.0060	0.6° from ⟨1 1 0⟩ direction
	179.4	0.5185	0.5242	0.6756	2.9° from the normal of {1 1 2} plane
	179.5	0.4737	0.4817	0.7373	2.9° from ⟨1 1 1⟩ direction
V2′ and V3′	85.0	0.7020	0.7120	0.0125	0.8° from ⟨1 1 0⟩ direction
	179.0	0.4745	0.4813	0.7371	2.9° from ⟨1 1 1⟩ direction
	179.5	0.5152	0.5271	0.6758	2.9° from the normal of {1 1 2} plane

Note: The rotation axes are expressed in coordinates; the *c*/*a* ratio should be taken into account when transforming the coordinates into the Miller indices.

Table 4. (a) Orientation relationships, expressed in terms of parallel planes and directions, between the nanotwins connected by the intralamellar interface as illustrated in Fig. 6a; (b and c) planes and directions in nanotwin variants V1′ (b) and V2′ (c) before and after the shear introduced by the assumed penetration of V4′ at the stepped intralamellar interface; subscript i' (i' = 1′, 2′, 3′, 4′) in the indices denotes that these indices are expressed with respect to the crystal coordinate system of Vi'.

Pair of nanotwins	Orientation relationship	
(a)		
V1′/V2′	$(1\,\bar{1}\,2)_{1'}//(\bar{1}\,\bar{1}\,2)_{2'}$	$[\bar{1}\,1\,1]_{1'}//[\bar{1}\,\bar{1}\,\bar{1}]_{2'}$
V3′/V4′	$(\bar{1}\,1\,2)_{3'}//(\bar{1}\,\bar{1}\,\bar{2})_{4'}$	$[1\,\bar{1}\,1]_{3'}//[\bar{1}\,\bar{1}\,1]_{4'}$
V1′/V3′	$(1\,\bar{1}\,2)_{1'}$ 5.9° from $(1\,\bar{1}\,2)_{3'}$	$[\bar{1}\,1\,1]_{1'}$ 5.8° from $[\bar{1}\,1\,1]_{3'}$
V1′/V4′	$(1\,\bar{1}\,\bar{2})_{1'}$ 5.7° from $(1\,1\,2)_{4'}$	$[\bar{1}\,1\,\bar{1}]_{1'}$ 5.7° from $[1\,1\,\bar{1}]_{4'}$
V2′/V3′	$(\bar{1}\,\bar{1}\,2)_{2'}$ 5.8° from $(1\,\bar{1}\,2)_{3'}$	$[1\,1\,1]_{2'}$ 5.8° from $[1\,\bar{1}\,\bar{1}]_{3'}$
V2′/V4′	Related to each other by a rotation of 15.8° around ⟨0.6995 0.7013 0.1371⟩ axis	

Plane before shear	Plane after shear	Direction before shear	Direction after shear
(b)			
$(\bar{1}\,1\,2)_{1'}$	$(\overline{0.9657}\,0.9647\,1.9146)_{1'}$ (0.2° from $(\bar{1}\,1\,2)_{1'}$)	$[1\,\bar{1}\,1]_{1'}$	$[0.9581\,\overline{0.9564}\,0.9651]_{1'}$ (0.2° from $[1\,\bar{1}\,1]_{1'}$)
$(\bar{1}\,\bar{1}\,2)_{1'}$	$(\overline{1.1563}\,\overline{0.8393}\,2.3886)_{1'}$ (8.2° from $(\bar{1}\,\bar{1}\,2)_{1'}$)	$[1\,1\,1]_{1'}$	$[0.7701\,1.2397\,0.8084]_{1'}$ (11.3° from $[1\,1\,1]_{1'}$)
$(1\,\bar{1}\,2)_{1'}$	$(0.6608\,\overline{0.6512}\,2.8433)_{1'}$ (21.2° from $(1\,\bar{1}\,2)_{1'}$)	$[\bar{1}\,1\,1]_{1'}$	$[\overline{1.4128}\,1.4303\,0.6559]_{1'}$ (21.3° from $[\bar{1}\,1\,1]_{1'}$)
$(1\,1\,2)_{1'}$	$(0.8515\,1.1528\,2.3693)_{1'}$ (7.8° from $(1\,1\,2)_{1'}$)	$[\bar{1}\,\bar{1}\,1]_{1'}$	$[\overline{1.2248}\,\overline{0.7657}\,0.8127]_{1'}$ (11.0° from $[\bar{1}\,\bar{1}\,1]_{1'}$)
(c)			
$(\bar{1}\,1\,2)_{2'}$	$(\overline{1.1005}\,0.9029\,1.6563)_{2'}$ (7.0° from $(\bar{1}\,1\,2)_{2'}$)	$[1\,\bar{1}\,1]_{2'}$	$[0.6937\,\overline{1.3175}\,1.1792]_{2'}$ (11.1° from $[1\,\bar{1}\,1]_{2'}$)
$(\bar{1}\,\bar{1}\,2)_{2'}$	$(\overline{1.2843}\,\overline{1.2746}\,1.0275)_{2'}$ (21.2° from $(\bar{1}\,\bar{1}\,2)_{2'}$)	$[1\,1\,1]_{2'}$	$[0.5225\,0.5050\,1.2794]_{2'}$ (21.2° from $[1\,1\,1]_{2'}$)
$(1\,\bar{1}\,2)_{2'}$	$(0.8930\,\overline{1.1033}\,1.6341)_{2'}$ (7.4° from $(1\,\bar{1}\,2)_{2'}$)	$[\bar{1}\,1\,1]_{2'}$	$[\overline{1.3003}\,0.6887\,1.1757]_{2'}$ (11.0° from $[\bar{1}\,1\,1]_{2'}$)
$(1\,1\,2)_{2'}$	$(1.0768\,1.0742\,2.2628)_{2'}$ (1.4° from $(1\,1\,2)_{2'}$)	$[\bar{1}\,\bar{1}\,1]_{2'}$	$[\overline{1.1290}\,\overline{1.1337}\,1.0755]_{2'}$ (1.4° from $[\bar{1}\,\bar{1}\,1]_{2'}$)

The detailed microstructure at the intralamellar interface is shown in Fig. 7. It is revealed that the intralamellar interface that is stepped in the SEM-BSE image (Fig. 2c) still possesses the "step" configuration in the TEM image, and no interpenetration is observed. This is quite different from the microstructure at the interlamellar interface. In fact, the calculation results from Eq. (1) (demonstrated in Table 4) show that the nanotwins meeting at the intralamellar interface also provide the possibility for penetration. However, no penetration actually occurs, as observed by TEM (Fig. 7). This suggests that the formation mechanism of the stepped intralamellar interface is different. It is quite probable that V1′/V2′ pair and V3′/V4′ pair do not form simultaneously, but one after the other. Suppose that V1′/V2′ forms before V3′/V4′. Constrained by the neighboring lamellae, the deformation strain due to the formation of V1′/V2′ accumulates at the interlamellar interface area and creates a resisting force in the opposite direction, which makes the formation of V3′/V4′ become energetically favorable. In this way, V3′/V4′ forms, leading to the reorientation of the martensitic lamellae, and consequently no interpenetration occurs at the intralamellar interface area. For clarification of the exact formation mechanism of the stepped intralamellar interface, further in-depth investigations are still needed.

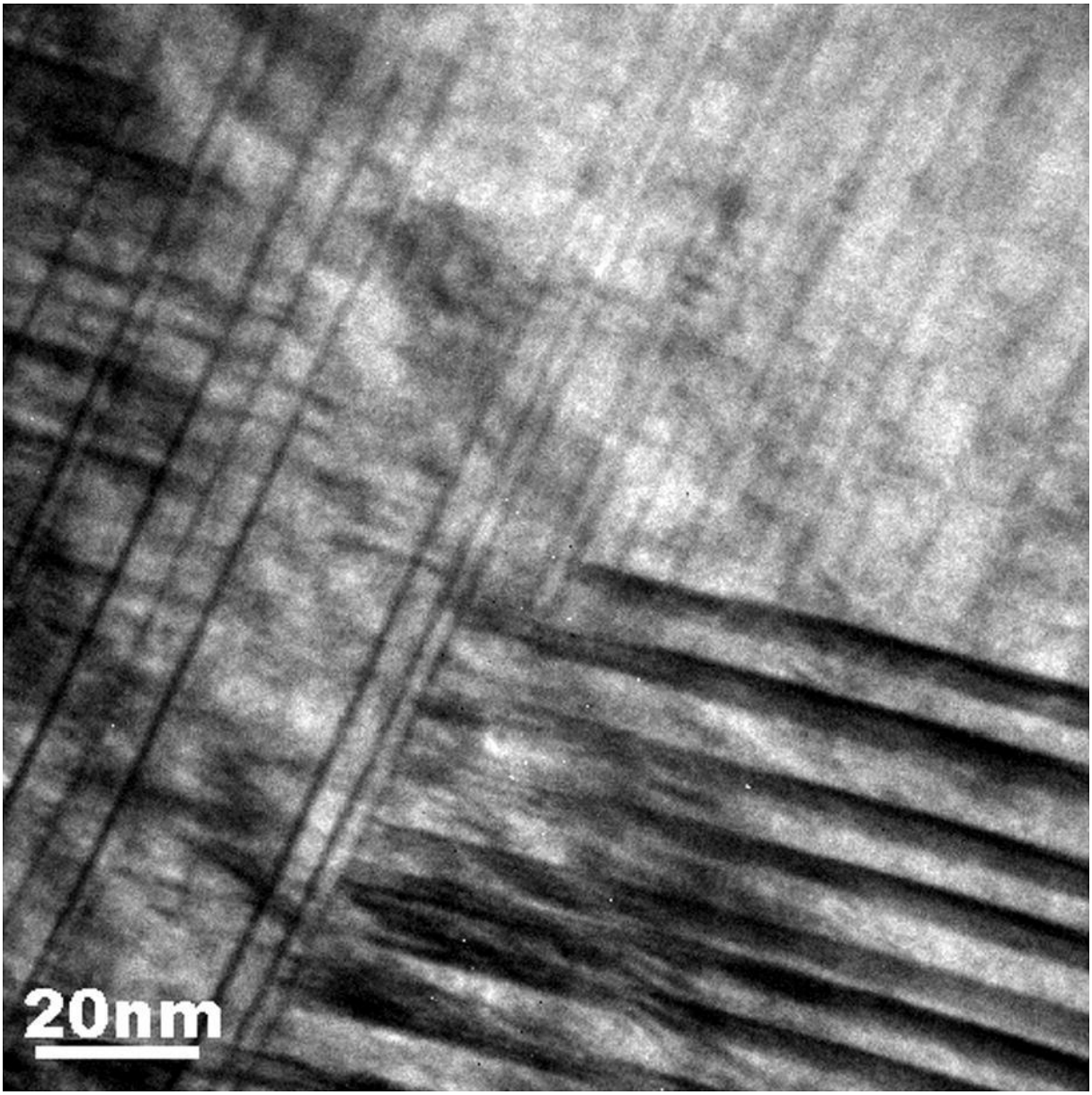

Fig. 7. TEM image showing the detailed microstructure at the stepped intralamellar interface.

4. Summary and conclusions

The microstructural and crystallographic features of the multiply twinned structure at the nanometer scale in a $Ni_{53}Mn_{25}Ga_{22}$ FSMA were studied in detail by means of experimental observation and calculations. The following conclusions can be drawn.

1.Nanoscale internal twins inside the micrometer-scale martensitic lamellae were found in the well self-accommodated microstructure.

2.In each martensitic lamella, there exist two internal nanotwin variants that have a compound twinning relationship between them. The twinning elements are $\mathbf{K_1} = \{112\}, \mathbf{K_2} = \{11\bar{2}\}, \boldsymbol{\eta_1} = \langle 11\bar{1}\rangle, \boldsymbol{\eta_2} = \langle 111\rangle, \mathbf{P} = \{1\bar{1}0\}$ and $s = 0.379$. The twin interface between the internal nanotwin variants is determined as {1 1 2}.

3.Two types of lamellar interfaces, i.e., interpenetrated interlamellar interface and stepped intralamellar interface, were revealed. The formation mechanisms of these two types of interfaces are different.

4.The orientation relationships between the nanotwins connected by the interlamellar and intralamellar interfaces were accurately determined. The individual orientation relationship between the neighboring nanotwins depends strongly on the adjacency condition at the lamellar interfaces.

The present work offers new insights into the correlation between microstructure and crystallography of FSMAs, and it is expected that these results could shed light on the microstructure design to improve the novel performances not only in FSMAs, but also in other advanced materials showing multiply twinned nanostructures.

Acknowledgements

The authors are grateful to the anonymous reviewer for constructive comments and suggestions. This work is supported by the National Natural Science Foundation of China (Nos. 50820135101, 50725102 and 50528102), the Cultivation Fund of the Key Scientific and Technical Innovation Project, Ministry of Education of China (No. 707017), the 111 Project (B07015) and the CNRS – PICS Project (No. 4164).

References

[1] Otsuka K, Wayman CM, editors. Shape memory materials. Cambridge: Cambridge University Press; 1998.

[2] Ren X, Otsuka K. Nature 1997;389:579.

[3] Huang X, Ackland GJ, Rabe KM. Nat Mater 2003;2:307.

[4] Bhattacharya K, Conti S, Zanzotto G, Zimmer J. Nature 2004;428:55.

[5] Liu YS, Xu D, Jiang BH, Yuan ZY, Van Houtte P. J Micromech Microeng 2005;15:575.

[6] Ullakko K, Huang JK, Kantner C, O'Handley RC, Kokorin VV. Appl Phys Lett 1996;69:1966.

[7] James RD, Wuttig M. Philos Mag A 1998;77:1273.

[8] Buschbeck J, Opahle I, Richter M, Rößler UK, Klaer P, Kallmayer M, et al. Phys Rev Lett 2009;103:216101.

[9] Karaca HE, Karaman I, Basaran B, Chumlyakov YJ, Maier HJ. Acta Mater 2006;54:233.

[10] Thomas M, Heczko O, Buschbeck J, Lai YW, McCord J, Kaufmann S, et al. Adv Mater 2009;21:3708.

[11] Aaltio I, Söderberg O, Ge Y, Hannula S-P. Scripta Mater 2010;62:9.

[12] Kaufmann S, Ro¨ßler UK, Heczko O, Wuttig M, Buschbeck J, Schultz L, et al. Phys Rev Lett 2010;104:145702.

[13] Chulist R, Oertel CG, Skrotzki W, Lippmann T. Scripta Mater 2010;62:235.

[14] Watanabe T, Tsurekawa S. Acta Mater 1999;47:4171.

[15] Söderberg O, Aaltio I, Ge Y, Heczko O, Hannula S-P. Mater Sci Eng A 2008;481–482:80.

[16] Diguet G, Beaugnon E, Cavaille´ JY. J Magn Magn Mater 2009;321:396.

[17] Sozinov A, Likhachev AA, Lanska N, Ullakko K. Appl Phys Lett 2002;80:1746.

[18] Murray SJ, Marioni MA, Kukla AM, Robinson J, O'Handley RC, Allen SM. J Appl Phys 2000;87:5774.

[19] Ge Y, Jiang H, Sozinov A, So¨derberg O, Lanska N, Keranen J, et al. Mater Sci Eng A 2006;438–440:961.

[20] Müllner P, Chernenko VA, Kostorz G. Scripta Mater 2003;49:129.

[21] Waitz T. Acta Mater 2005;53:2273.

[22] Söderberg O, Ge Y, Sozinov A, Hannula S-P, Lindroos VK. Smart Mater Struct 2005;14:S223.

[23] Han M, Bennett JC, Gharghouri MA, Chen J, Hyatt CV. Acta Mater 2007;55:1731.

[24] Mahnke GJ, Seibt M, Mayr SG. Phys Rev B 2008;78:012101.

[25] Meng XL, Sato M, Ishida A. Acta Mater 2008;56:3394.

[26] Scheerbaum N, Heczko O, Liu J, Hinz D, Schultz L, Gutfleisch O. New J Phys 2008;10:73002.

[27] Scheerbaum N, Lai YW, Leisegang T, Thomas M, Liu J, Khlopkov K, et al. Acta Mater 2010;58:4629.

[28] Chopra HD, Ji C, Kokorin VV. Phys Rev B 2000;61:R14913.

[29] Chmielus M, Zhang XX, Witherspoon C, Dunand DC, Mïullner P. Nat Mater 2009;8:863.

[30] Scheerbaum N, Hinz D, Gutfleisch O, Skrotzki W, Schultz L. J Appl Phys 2007;101:09C501.

[31] Chmielus M, Glavatskyy I, Hoffmann JU, Chernenko VA, Schneider R, Mu¨ llner P. Scripta Mater 2011;64:888.

[32] Gaitzsch U, Po¨tschke M, Roth S, Rellinghaus B, Schultz L. Acta Mater 2009;57:365.

[33] Lai YW, Scha¨fer R, Schultz L, McCord J. Acta Mater 2008;56:5130.

[34] Bechtold C, Gerber A, Wuttig M, Quandt E. Scripta Mater 2008;58:1022.

[35] Ge Y, Heczko O, Söderberg O, Hannula S-P. Scripta Mater 2006;54:2155.

[36] Lai YW, Scheerbaum N, Hinz D, Gutfleisch O, Schäfer R, Schultz L, et al. Appl Phys Lett 2007;90:192504.

[37] Straka L, Lanska N, Ullakko K, Sozinov A. Appl Phys Lett 2010;96:131903.

[38] Chulist R, Skrotzki W, Oertel CG, Bo¨hm A, Po¨tschke M. Scripta Mater 2010;63:548.

[39] Pons J, Chernenko VA, Santamarta R, Cesari E. Acta Mater 2000;48:3027.

[40] Righi L, Albertini F, Pareti L, Paoluzi A, Calestani G. Acta Mater 2007;55:5237.

[41] Wang WH, Liu ZH, Zhang J, Chen JL, Wu GH, Zhan WS, et al. Phys Rev B 2002;66:052411.

[42] Ranjan R, Banik S, Barman SR, Kumar U, Mukhopadhyay, Pandey D. Phys Rev B 2006;74:224443.

[43] Righi L, Albertini F, Villa E, Paoluzi A, Calestani G, Chernenko V, et al. Acta Mater 2008;56:4529.

[44] Brown PJ, Crangle J, Kanomata T, Matsumoto M, Neumann KU, Ouladdiaf B, et al. J Phys: Condens Matter 2002;14:10159.

[45] Cong DY, Zetterstro¨m P,Wang YD, Delaplane R, Peng RL, Zhao X, et al. Appl Phys Lett 2005;87:111906.

[46] Cong DY, Wang YD, Xu JZ, Zuo L, Zetterström P, Delaplane R. Powder Diffr 2007;22:307.

[47] Khachaturyan AG, Shapiro SM, Semenovskaya S. Phys Rev B 1991;43:10832.

[48] Chernenko VA, Chmielus M, Mu¨ llner P. Appl Phys Lett 2009;95:104103.

[49] Morito H, Oikawa K, Fujita A, Fukamichi K, Kainuma R, Ishida K.Scripta Mater 2010;63:379.

[50] Masdeu F, Pons J, Cesari E, Kustov S, Chumlyakov. Appl Phys Lett 2008;93:152503.

[51] Morito H, Fujita A, Oikawa K, Ishida K, Fukamichi K, Kainuma R. Appl Phys Lett 2007;90:062505.

[52] Ma YQ, Yang SY, Liu Y, Liu XJ. Acta Mater 2009;57:3232.

[53] Chernenko VA, L'vov V, Pons J, Cesari E. J Appl Phys 2003;93:2394.

[54] Xu H, Ma Y, Jiang C. Appl Phys Lett 2003;82:3206.

[55] Khovaylo V, Kainuma R, Ishida K, Omori T, Miki H, Takagi T, et al. Philos Mag 2008;88:865.

[56] Xin Y, Li Y, Liu ZD. Scripta Mater 2010;63:35.

[57] Penelle R. Int J Mater Res 2009;100:1420.

[58] Dillien S, Seefeldt M, Allain S, Bouaziz O, Van Houtte P. Mater Sci Eng A 2010;527:947.

[59] Tsurekawa S, Ibaraki K, Kawahara K, Watanabe T. Scripta Mater 2007;56:577.

[60] Chulist R, Skrotzki W, Oertel CG, Bo¨hm A, Lippmann T, Rybacki E. Scripta Mater 2010;62:650.

[61] Chulist R, Po¨tschke M, Lippmann T, Oertel CG, Skrotzki W. J Phys: Conf Ser 2010;240:012024.

[62] Hürrich C, Wendrock H, Po¨tschke M, Gaitzsch U, Roth S,

Rellinghaus B, et al. J Mater Eng Perform 2009;18:554.

[63] Koblischka-Veneva A, Gachot C, Leibenguth P, Mu¨cklich F. J Magn Magn Mater 2007;316:e431.

[64] Cong DY, Zhang YD, Wang YD, Esling C, Zhao X, Zuo L. J Appl Crystallogr 2006;39:723.

[65] Zhang YD, Esling C, Zhao X, Zuo L. J Appl Crystallogr 2007;40:436.

[66] So¨derberg O, Straka L, Nova´k V, Heczko O, Hannula S-P, Lindroos VK. Mater Sci Eng A 2004;386:27.

[67] Christian JW, Mahajan S. Prog Mater Sci 1995;39:1.

[68] Kelly A, Groves GW. Crystallography and crystal defects. London: Longman Press; 1970.

[69] Mahajan S. Deformation twinning. Encyclopedia of Materials:

Science and Technology; 2008. p. 1–14.